Control of Transitional and Turbulent Flows Using Plasma-Based Actuators

Miguel R. Visbal* & **Datta V. Gaitonde†**
Computational Sciences Branch
Air Vehicles Directorate
Air Force Research Laboratory
Wright-Patterson AFB, OH 45433

Subrata Roy‡
Computational Plasma Dynamics Laboratory
Department of Mechanical Engineering
Kettering University
Flint, MI 48504

An exploratory numerical study of the control of transitional and turbulent separated flows by means of asymmetric dielectric-barrier-discharge (DBD) actuators is presented. The flow fields are simulated employing an extensively validated high-fidelity Navier-Stokes solver which is augmented with both phenomenological and first-principles models representing the plasma-induced body forces imparted by the actuator on the fluid. Several applications are considered, including suppression of wing stall, control of boundary layer transition on a plate, control of laminar separation over a ramp, and turbulent separation over a wall-mounted hump. Effective suppression of stall over a NACA 0015 airfoil at moderate Reynolds numbers is demonstrated using either co-flow or counter-flow *pulsed* actuators with sufficiently high frequency. By contrast, continuous actuation (simulated by a steady body force in the phenomenological model) is found to provide little control of separation. For continuous actuator operation, the first-priciples approach is needed in order to reproduce the benefits of the inherently unsteady force induced by the plasma actuator. The pulsed-modulated unsteady plasma force is found to be more effective than a monochromatic radio-frequency forcing. These results highlight the greater importance of transition and turbulence enhancement mechanisms rather than pure wall-jet momentum injection for the effective use of DBD devices. As a consequence, meaningful computations require the use of three-dimensional large-eddy simulation approaches capable of capturing the effects of unsteady forcing on the transitional/turbulent flow structure. For a laminar boundary layer developing along a flat plate, a counter-flow DBD actuator is shown to provide an effective on-demand tripping device . This property is exploited for the suppression of laminar separation over a ramp. It is demonstrated that tripping of the laminar boundary layer upstream of the adverse pressure gradient is more effective than forcing of the separated shear layer. This behavior may be beneficial in the control of laminar flow wings and low-pressure turbines. Control of turbulent boundary-layer separation over a wall-mounted hump suggests that once the flow is turbulent, control effectiveness is only achieved provided the actuator strength exceeds a certain threshold. This finding has implications for the scalability of DBD devices to higher freestream velocities encountered in practical applications.

I. INTRODUCTION

Control of subsonic flows employing plasma-induced body forces is currently a topic of considerable interest. This is motivated by several distinct advantages associated with plasma actuators, including: the absence of complicated mechanical or pneumatic systems, their operation over a broad range of frequencies, as well as their relative low power consumption. The specific plasma-based technique being considered here is the so-called single asymmetric

*Tech. Area Leader, Associate Fellow AIAA
†Tech. Area Leader, Associate Fellow AIAA
‡Associate Professor, Associate Fellow AIAA.

dielectric-barrier-discharge (or DBD) actuator, which typically operates in the low radio frequency range (1-10KHz), with voltage amplitudes of 5-10KV. A schematic of a DBD actuator is shown in Fig. 1a. Velocity measurements[1] indicate that the averaged plasma-induced body forces results is the formation of a wall jet. A recent overview of the design, optimization and application of DBD actuators has been given by Corke and Post.[2] Experiments have shown the potential of DBD actuators for the control of boundary-layer separation on both external and internal flows.[1,3–6] Computational studies on the application of these plasma actuators have also been presented.[7–11]

Despite significant advances in the understanding of DBD actuator effects, further work is still needed in order to construct detailed models for the spatio-temporal distribution of the plasma-induced body forces suitable for incorporation into high-fidelity viscous flow simulations. In addition, new strategies aimed at exploiting these devices in the control of complex three-dimensional flows should be explored.

The present work examines the control of separated flows utilizing simulated DBD actuators. Since the flow fields of interest are typically characterized by transition and turbulence, a high-fidelity three-dimensional viscous methodology is required. This high-end flow simulation technique is computationally intensive, and therefore, a first-principles fully-coupled approach of the plasma effects, even if available, becomes prohibitive. For this reason, at this stage, the plasma-induced body forces are represented using either a phenomenological model[8,11] or a loosely-coupled first-principles approach.[12,13] These methods represent respectively the averaged and instantaneous force introduced by the actuator in a specified plasma region above the device.

This work is focused on the identification of strategies for effective flow control of transitional and turbulent separated flows using DBD devices. To this end, the critical role of pulsed-modulated actuators in providing a source of unsteady forcing is examined. Emphasis is placed on the greater importance of unsteady forcing rather than pure streamwise momentum injection as the primary control mechanism. With the exception of very low freestream velocities or very strong wall jet effects, transition/turbulence enhancements are shown to be the dominant mechanism. The present emphasis also dictates the use of a high-fidelity three-dimensional computational approach capable of describing the impact of unsteady forcing on the spatio-temporal transition/turbulence structure.

To highlight the key mechanisms, a comprehensive set of applications is considered, including suppression of wing stall, control of boundary layer transition on a plate, control of laminar separation over a ramp, and turbulent separation over a wall-mounted hump. A comparison of the phenomenological and first-principles approaches for wing stall supression using a continuously-powered actuator is also presented.

II. Governing equations

The flow field is assumed to be described by the full Navier-Stokes equations, augmented by terms representing the local forcing of the DBD device.[11] In non-dimensional form, the mass, momentum and energy equations are:

$$\frac{\partial \rho^*}{\partial t^*} + \nabla^* \cdot \left(\rho^* \vec{U}^* \right) = 0 \tag{1}$$

$$\frac{\partial \rho^* \vec{U}^*}{\partial t^*} + \nabla^* \cdot \left[\rho^* \vec{U}^* \bar{\vec{U}}^* + p^* \bar{\bar{I}} \right] - \frac{1}{Re} \nabla^* \cdot \bar{\bar{\tau}}^* = D_c q_c^* \vec{E}^* \tag{2}$$

$$\frac{\partial \rho^* e^*}{\partial t^*} + \nabla^* \cdot \left[\left(\rho^* e + p^* \right) \vec{U}^* - \frac{1}{Re} \left(\vec{U}^* \cdot \bar{\bar{\tau}}^* \right) - \frac{1}{(\gamma - 1) PrM^2 Re} Q_{ht}^* \right] = D_c q_c^* \vec{U}^* \cdot \vec{E}^* \tag{3}$$

where the superscript $*$ denotes a non-dimensional quantity, and $\vec{U}^* = \{u^*, v^*, w^*\}$, ρ^*, p^*, e^* and t^* represent the velocity vector, density, static pressure, total energy and time respectively. $\bar{\bar{\tau}}$ denotes the shear stress tensor, Q_{ht}^* is the heat conduction term, q_c^* is the charge density and $\vec{E}^* = \left\{ E_x^*, E_y^*, E_z^* \right\}$ is the electric field vector. The manner in which the distributions of charge density and the electric field are obtained is described below. The non-dimensionalization is accomplished through the following relations:

$$t^* = \frac{tU_{ref}}{L} \quad \rho^* = \frac{\rho}{\rho_{ref}} \quad U^* = \frac{U}{U_{ref}} \quad p^* = \frac{p}{\rho_{ref} U_{ref}^2} \quad \mu^* = \frac{\mu}{\mu_{ref}} \quad T^* = \frac{T}{T_{ref}} \tag{4}$$

where the subscript ref denotes reference values. Several non-dimensional parameters appear, including the Reynolds number $Re = \frac{\rho_{ref} U_{ref} L_{ref}}{\mu_{ref}}$, the Prandtl number $Pr = \frac{\mu_{ref} C_p}{k_{ref}} = 0.72$ and the Mach number $M = \frac{U_{ref}}{\sqrt{\frac{\gamma p_{ref}}{\rho_{ref}}}}$. The molecular viscosity, μ is obtained from Sutherland's law, and a perfect gas is assumed.

The parameter D_c, representing the scaling of the electrical to inertial forces is given by:

$$D_c = \frac{q_{c,ref} E_{ref} L_{ref}}{\rho_{ref} U_{ref}^2} \tag{5}$$

In the subsequent discussion, the superscript (*) is dropped and all quantities are assumed to be non-dimensional unless stated otherwise.

The governing equations may be written in flux vector form as:

$$\frac{\partial X}{\partial t} + \frac{\partial F_I}{\partial x} + \frac{\partial G_I}{\partial y} + \frac{\partial H_I}{\partial z} = \frac{\partial F_V}{\partial x} + \frac{\partial G_V}{\partial y} + \frac{\partial H_V}{\partial z} + S \tag{6}$$

where X is the solution vector, $X = \{\rho, \rho u, \rho v, \rho w, \rho e\}$, F_I, G_I, and H_I represent terms relevant to inviscid, perfectly conducting media while F_V, G_V, and H_V include effects due to viscosity.

The source vector, S contains the terms pertinent to the DBD forcing and may be derived either from models incorporating various degrees of phenomenological and first-principles components.[11,12] In order to treat physically complex domains, the above governing equations are extended to curvilinear coordinates in the standard manner[14] by introducing the transformation $x = x(\xi, \eta, \zeta)$, $y = y(\xi, \eta, \zeta)$, $z = z(\xi, \eta, \zeta)$. The strong conservation form is thus obtained:

$$\frac{\partial \hat{X}}{\partial t} + \frac{\partial \hat{F}_I}{\partial \xi} + \frac{\partial \hat{G}_I}{\partial \eta} + \frac{\partial \hat{H}_I}{\partial \zeta} = \frac{\partial \hat{F}_V}{\partial \xi} + \frac{\partial \hat{G}_V}{\partial \eta} + \frac{\partial \hat{H}_V}{\partial \zeta} + \hat{S} \tag{7}$$

where J represents the Jacobian of the transformation, $\hat{X} = X/J$, $\hat{S} = S/J$ and,

$$\begin{aligned} \hat{F}_I &= \frac{1}{J}(\xi_x F_I + \xi_y G_I + \xi_z H_I) \\ \hat{F}_V &= \frac{1}{J}(\xi_x F_V + \xi_y G_V + \xi_z H_V) \end{aligned}$$

with similar expressions for the remaining flux vectors.

Unless otherwise noted, the effect of the plasma actuator is modeled employing a phenomenological approach. The body force is obtained by specifying both the charge distribution and the spatial variation of the mean electric field. The general development follows that described by Shyy *et al.*[8] However, to factor uncertainties in the model, and to explore the sensitivity of the fully separated flow to different force distributions, additional parameters are introduced to permit variations in force orientation and strength.[11] Although this approach is empirical, it provides an attractive framework to explore plasma-based control of complex three-dimensional flows. The parameters describing the simulated body forces are the actuator strength D_c, as well as the normal and streamwise dimensions of the plasma region (a, b in Fig. 1a). These parameters are given later for each case considered.

Although the DBD actuator is inherently an unsteady device, the body-force imposed on the fluid in the *phenomenological* model is considered to be steady given the high frequency of the applied voltage (typically of order 5-10kHz). Therefore this situation represents an actuator which is being powered continuously. In order to reduce power consumption, the actuator may be operated in a pulsed manner, as described in Ref. 2. As it will be shown later, even more important than actuator power considerations is the fact that a pulsed mode of operation introduces lower forcing frequencies to which the flow is more receptive and offers the potential of improved control effectiveness. For a simulated pulsed actuator, the force amplitude is modulated according to the duty cycle shown in Fig. 1b where T_p denotes the fundamental period and T_d the portion of the cycle over which the actuator is switched on. The duty cycle is typically expressed as the percentage $T_d/T_p \times 100\%$. It should be noted that in addition to the imposed primary frequency $f_p = 1/T_p$, this waveform introduces multiple harmonics, as shown in the signal spectrum of Fig. 1c. In all cases described below, a 50 % duty cycle is employed.

Finally, as described in Section IV.B, a first-principles approach[12,13] is also considered for the control of stall over a wing.

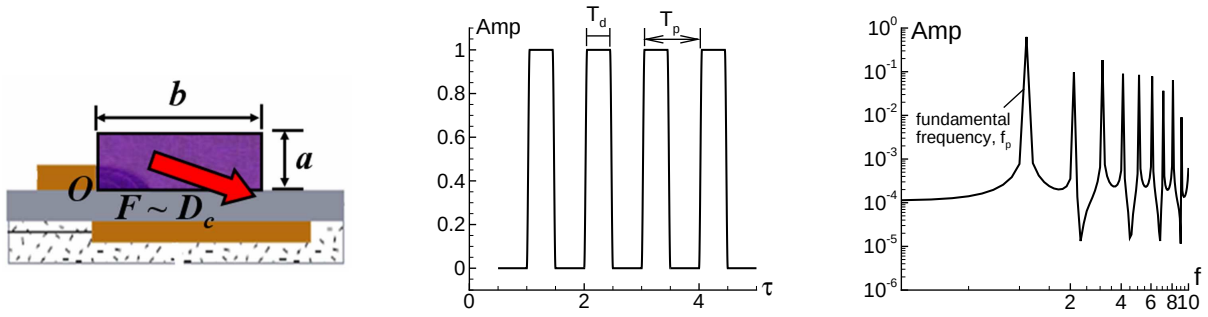

(a) (b) (c)

Figure 1. (a) Schematic of DBD actuator, (b) pulsed actuator duty cycle, and (c) spectrum of imposed forcing amplitude

III. NUMERICAL METHODOLOGY

All of the simulations described in this work are computed with the extensively validated high-order Navier-Stokes solver *FDL3DI*.[15,16] In this code, a finite-difference approach is employed to discretize the governing equations, and all spatial derivatives are obtained with high-order compact-differencing schemes.[17] For any scalar quantity, ϕ, such as a metric, flux component or flow variable, the spatial derivative ϕ' is obtained along a coordinate line in the transformed plane by solving the tridiagonal system:

$$\alpha\phi'_{i-1} + \phi'_i + \alpha\phi'_{i+1} = \beta\frac{\phi_{i+2} - \phi_{i-2}}{4} + \gamma\frac{\phi_{i+1} - \phi_{i-1}}{2} \tag{8}$$

where α, γ and β determine the spatial properties of the algorithm. For all the computations reported in this paper, a sixth-order scheme (*C6*) is used corresponding to $\alpha = \frac{1}{3}$, $\gamma = \frac{14}{9}$ and $\beta = \frac{1}{9}$. At boundary points, higher-order one-sided formulas are utilized which retain the tridiagonal form of the scheme.[15,16] Typically, Neumann boundary conditions are implemented with third-order one-sided expressions.

The derivatives of the inviscid fluxes are obtained by forming the fluxes at the nodes and differentiating each component with the above formula. Viscous terms are obtained by first computing the derivatives of the primitive variables. The components of the viscous flux are then constructed at each node and differentiated by a second application of the same scheme. In curvilinear coordinates, this approach is significantly cheaper to implement than that in which a Pade-type scheme is employed directly for the second-order derivatives.[15]

In order to eliminate spurious components, a high-order low-pass spatial filtering technique[15,18] is incorporated. If a typical component of the solution vector is denoted by ϕ, filtered values $\hat{\phi}$ at interior points in transformed space satisfy,

$$\alpha_f\hat{\phi}_{i-1} + \hat{\phi}_i + \alpha_f\hat{\phi}_{i+1} = \Sigma_{n=0}^{N}\frac{a_n}{2}\left(\phi_{i+n} + \phi_{i-n}\right) \tag{9}$$

Equation (9) is based on templates proposed in Refs. 17 and 19 and with proper choice of coefficients, provides a $2N$th-order formula on a $2N+1$ point stencil. The $N+1$ coefficients, $a_0, a_1, \ldots a_N$, are derived in terms of α_f using Taylor- and Fourier-series analyses. These coefficients, along with representative filter transfer functions, can be found in Refs. 20 and 16. The filter is applied to the conserved variables along each transformed coordinate direction once after each time step or sub-iteration. For the near-boundary points, the filtering strategies described in Refs. 15 and 20 are used. For the present study, a minimum eighth-order filter operator is applied with $\alpha_f \geq 0.3$. For transitional and

turbulent flows, the previous high-fidelity spatial algorithmic components provide an effective implicit LES (*ILES*) approach in lieu of traditional sub-grid-scale models, as demonstrated in Refs. 21 and 22. Finally, time-marching is accomplished by incorporating an iterative, implicit approximately-factored procedure.[21,22]

IV. RESULTS

A. Control of Wing Stall

Control of the stalled flow past a NACA 0015 airfoil has been investigated. The Mach number, chord Reynolds number and angle of attack are chosen as $M_\infty = 0.1$, $Re_c = 45,000$ and $\alpha = 15^o$, respectively. This particular case was previously considered in Ref. 11. In the present work, both pulsed co-flow and counter-flow actuators located near the separation point are used. In addition, much smaller plasma forces are prescribed in order to demonstrate control effectiveness by promoting transition and turbulence.

The airfoil flows were simulated on a $308 \times 145 \times 75$ O-grid. The flow was assumed to be periodic in the spanwise direction, with a span equal to $0.2c$. The time step was chosen as $\Delta t U_\infty / c = 0.00025$ which provided 500 time steps per cycle for the highest duty-cycle frequency considered.

The global structure of the baseline and controlled flow fields is shown in Fig. 2 in terms of streamwise velocity and spanwise vorticity contours. At this high incidence, the baseline flow is observed to be fully stalled. Laminar boundary layer separation takes place very close to the airfoil leading edge (Fig. 2a). This process results in the formation of a free shear layer which, for this moderate Reynolds number and high angle of attack, fails to transition rapidly in order to provide re-attachment. The time-averaged velocity contours (Fig. 2b) display a separation zone which extends significantly in the direction normal to the wing section. The extent of separation can be seen more clearly in Fig. 3c which shows the mean streamwise velocity profile at a station near mid-chord ($x/c = 0.42$). As a result of this massive separation zone, the mean surface pressure (Fig. 3b), displays a flat distribution along the upper surface, typical of a fully stalled flow.

Control of the stalled airfoil flow was investigated employing both steady and pulsed, as well as co-flow and counter-flow DBD actuators. For all cases, the actuator origin was placed at $x/c = 0.024$, just downstream of the mean boundary-layer separation location for the baseline flow. The geometric parameters of the simulated plasma region were taken to be $a/c = 0.005$ and $b/c = 0.03$. A summary of all the cases considered, as well as the corresponding actuator strength (D_c), orientation and duty-cycle primary frequency are provided in Table 1.

Control	D_c	$St_p = f_p c/U_\infty$	$C_{L_{mean}}$	$(L/D)_{mean}$
baseline	0.0	0.0	0.79	2.87
co-flow	75.0	0.0	0.7	3.15
co-flow	150.0	0.0	0.71	3.13
co-flow	75.0	4.0	1.12	12.10
co-flow	150.0	4.0	1.20	14.02
counter-flow	75.0	0.0	0.56	2.15
counter-flow	75.0	4.0	0.96	10.47
counter-flow	150.0	1.0	0.92	5.53
counter-flow	150.0	2.0	0.93	8.92
counter-flow	150.0	4.0	1.02	11.05
counter-flow	150.0	8.0	1.05	11.80

Table 1. Summary of airfoil cases and actuator parameters

The use of a steady (*i.e.* continuous) co-flow actuator with $D_c = 75.0$ and 150.0 was considered first. The

corresponding overall flow structure for $D_c = 150.0$ is shown in Fig. 2. Examination of the transient response of the flow following the onset of actuation indicated that, initially, a significant downstream diplacement of the separation point takes place due to the actuator-induced streamwise wall jet. The nature of this transient response is illustrated in Fig. 3a which shows the history of the streamwise velocity component near the surface at a station just upstream of the actuator ($x/c = 0.007$). During the early stages of actuation, the velocity is observed to increase significantly, as the flow reattaches in the front part of the airfoil. However, despite this beneficial transient effect of the wall jet entrainment, the flow eventually returns to a completely stalled condition (Fig. 2a,b). After a time-asymptotic state is reached, the mean separation location near the leading edge has shifted downstream (from $x/c \approx 0.02$ to $x/c \approx 0.046$) and consequently there is a small decrease in the initial angle formed by the free shear relative to the airfoil (Fig. 2c). However, near mid-chord the normal extent of the reversed flow region remains effectively unchanged (see Fig. 3c). The airfoil mean surface pressure (Fig. 3b) also displays little improvement relative to the baseline case, with the exception of a small localized suction peak in the vicinity of the actuator. Comparison of the C_p-distributions and velocity profiles (Fig. 3b,c) for $D_c = 75.0$ and $D_c 150.0$ shows no significant improvement with increasing actuator strength below a certain threshold. Therefore, steady actuation (modeled with the phenomenological approach) is found to be ineffective for the actuator strength parameters considered. It should be noted that for a value of D_c an order-of-magnitude larger, the simulated steady actuator was found[11] previously to fully attach the flow due to the presence of a very strong wall jet. The present results suggest that a steady actuator force of limited magnitude is not an effective means of flow control, and attempts to attach the boundary layer through pure streamwise momentum injection are therefore of limited applicability. In order to exploit the receptivity of the flow to unsteady disturbances, we turn our attention to the case of a pulsed actuator.

The case of a pulsed co-flow actuator with $D_c = 75.0$ and a primary duty-cycle non-dimensional frequency $St_p = f_p c/U_\infty = 4.0$ was considered. As shown in Figs. 2a,b, the pulsed actuation reattaches the separated flow, and much higher streamwise mean velocities are observed above the airfoil upper surface as the flow turns completely around the leading edge. The mean C_p distribution (Fig. 3b) for this streamlined flow exhibits a well-defined suction peak which reflects in a significant increase in lift coefficient and lift-to-drag ratio (see Table 1). The velocity profile near mid-chord (Fig. 3c) displays also a fully-attached character. Examination of the instantaneous spanwise vorticity contours in Figs. 2c,d indicates that the pulsed force engenders a rapid transition to turbulence of the initially laminar shear layer which promotes a mean attached flow.

In order to contrast the relative importance of transition and turbulence enhacement mechanisms relative to simple wall-jet momentum injection arguments, the impact of a counter-flow actuator was also explored. A steady counter-flow actuator resulted, as expected, in further degradation of the baseline stalled flow. This can be observed in terms of the surface presssure distribution and velocity profile (Fig. 4), as well as in the mean aerodynamic loads (Table 1). By contrast, the use of a pulsed counter-flow actuator (with $D_c = 75.0$ and $St_p = 4.0$) was found to be very effective in eliminating stall, as clearly seen in Figs. 2a,b. This control is again achieved by the rapid transition of the shear layer downstream of a small separation bubble generated by the counter-flow actuator.[23] The pulsed counter-flow actuator was found to be slightly more effective when doubling the strength parameter to $D_c = 150.0$ (see Table 1). This further emphasizes the importance of unsteady forcing rather than momentum injection as the primary control mechanism.

The effect of pulsing frequency was considered for the counter-flow actuator with a strength parameter $D_c = 150.0$. The duty-cycle frequency was varied over the range $1.0 \leq St_p \leq 8.0$. A comparison of the instantaneous flow fields obtained with the lowest and highest pulsing frequency is shown in Fig. 5. Also, the time-averaged surface pressure and velocity profiles at $x/c = 0.42$ are displayed for all values of St_p in Fig. 6. Although with $St_p = 1.0$ the flow begins to transition downstream of the actuator (Figs. 5b,c), the process is not as effective as for the case of high-frequency pulsing. With $St_p = 8.0$, the shear layer quickly breakdowns due to spanwise instabilities, and much higher values of vorticity are observed near the wing surface. The mean surface C_p (Fig. 6a) exhibits the development of a stronger suction peak with increasing frequency, however this effect seems to saturate after $St_p = 4.0$. Comparison of the velocity profiles (Fig. 6b) shows a reduction of the boundary layer displacement with increasing St_p. The beneficial effects of high-frequency pulsing are also evident in the improvements of mean lift coefficient and L/D seen in Table 1.

The control mechanism of the pulsed counter-flow actuator is further examined in reference to the instantaneous

vortical structure shown in Fig. 5a. In each cycle of the pulsing, a dynamic-stall-like vortex[24] is generated near the leading edge downstream of the actuator. For the higher duty-cycle frequency ($St_p = 8.0$), this leading-edge vortex forms closer to the actuator and to the airfoil surface. The actuator-induced vortex is observed to be initially coherent but quickly breakdowns due to spanwise instabilities, as it convects along the airfoil upper surface. It therefore appears that the increased control effectiveness of the pulsed actuator derives from the process of modulated vorticity injection. This behavior is in some respects similar to that observed in flow control experiments employing high-frequency synthetic jets (see Ref. 25 and references therein).

Although additional computations are required in order to provide guidance for optimal control effectiveness, the previous exploratory results serve to highlight the greater importance of unsteady forcing versus pure wall jet momentun injection in the effective use of DBD actuators for flow control.

As noted earlier, even for a continuous actuator the imposed plasma forces are inherently unsteady. Given the importance of unsteady forcing on the flow evolution, and the fact that for a continuous actuator this effect cannot be accounted for with a phenomenological model, we consider next the use a first-principles approach.

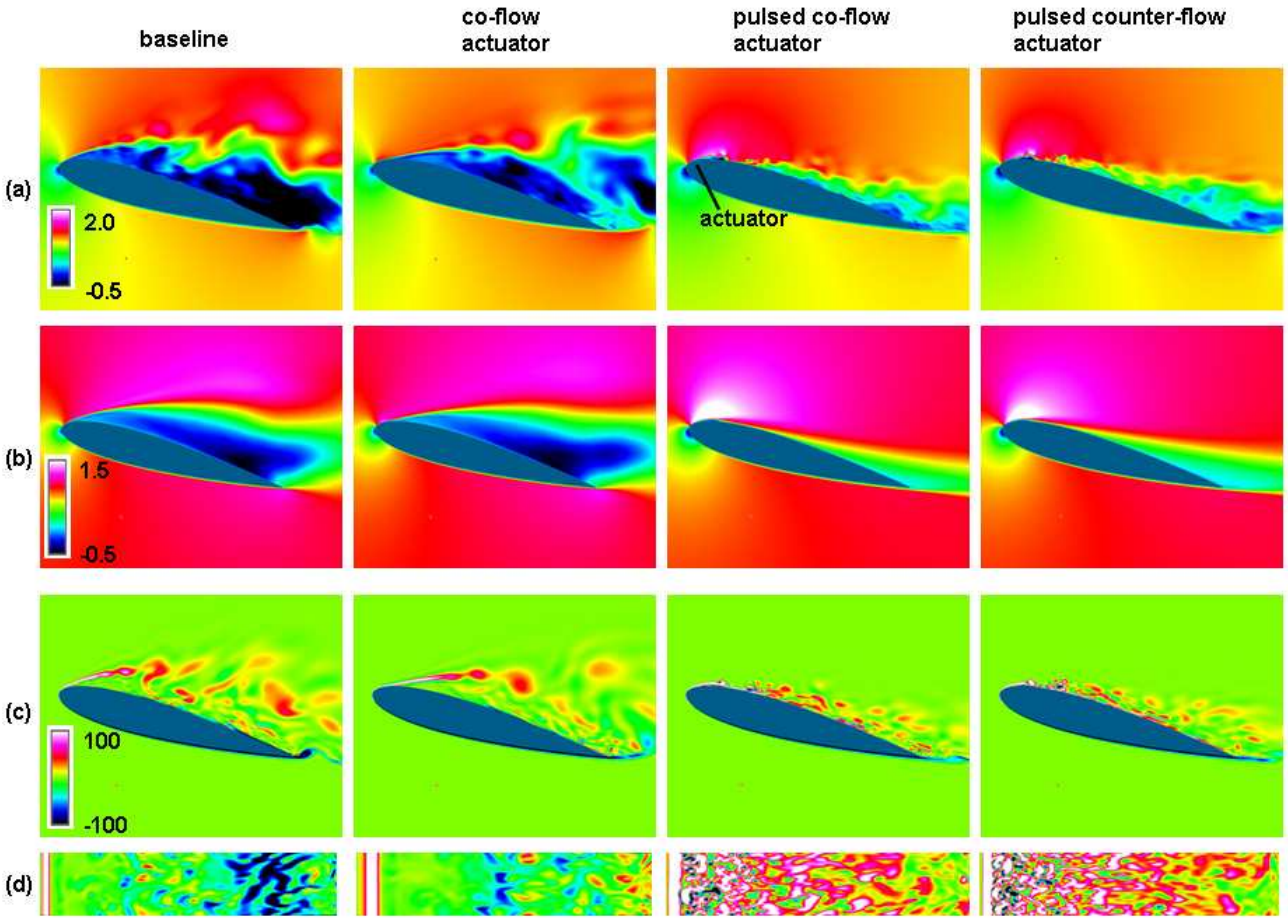

Figure 2. Effect of DBD actuator on stalled flow above a NACA 0015 wing section ($Re_c = 4.5 \times 10^4, \alpha = 15^o$): (a) instantaneous and (b) mean streamwise velocity; spanwise vorticity on (c) vertical plane, and (d) on plane parallel to airfoil surface

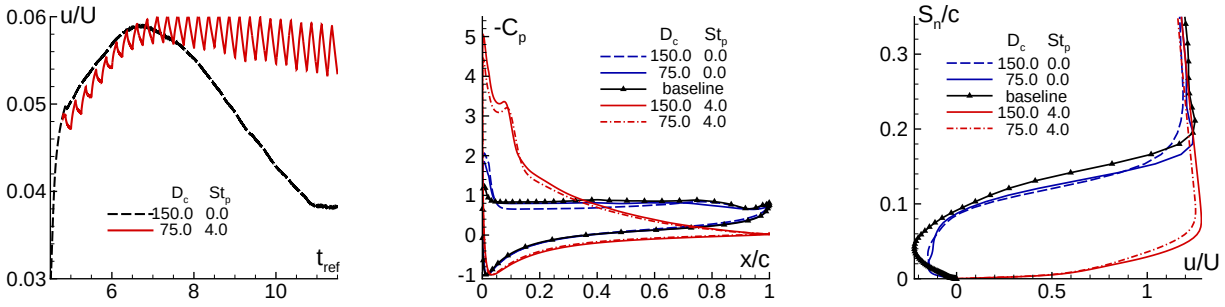

(a) (b) (c)

Figure 3. Effect of *co-flow* actuator on NACA 0015 airfoil flow ($Re_c = 4.5 \times 10^4, \alpha = 15^o$) : (a) history of streamwise velocity near leading edge, (b) mean surface pressure, and (c) time-averaged velocity profile near mid-chord

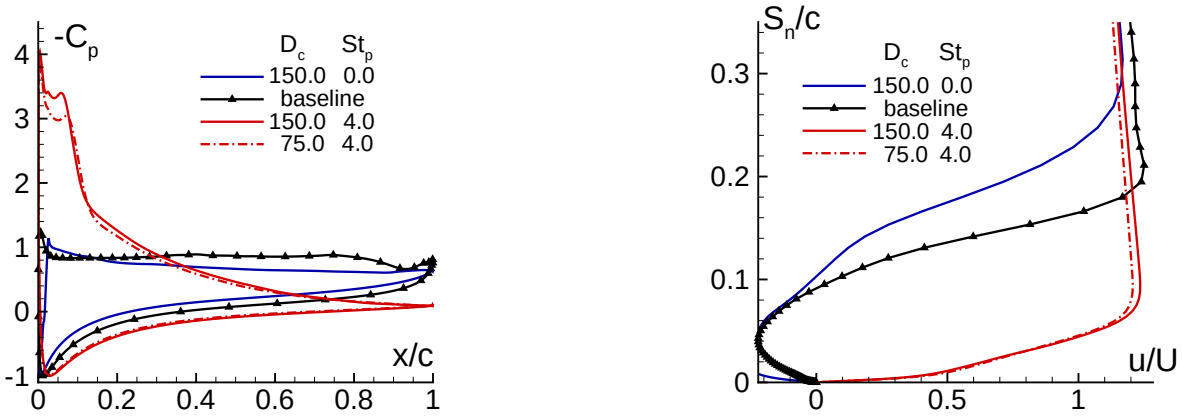

(a) (b)

Figure 4. Effect of *counter-flow* actuator on NACA 0015 airfoil flow ($Re_c = 4.5 \times 10^4, \alpha = 15^o$): (a) mean surface pressure, and (b) time-averaged velocity profile near mid-chord

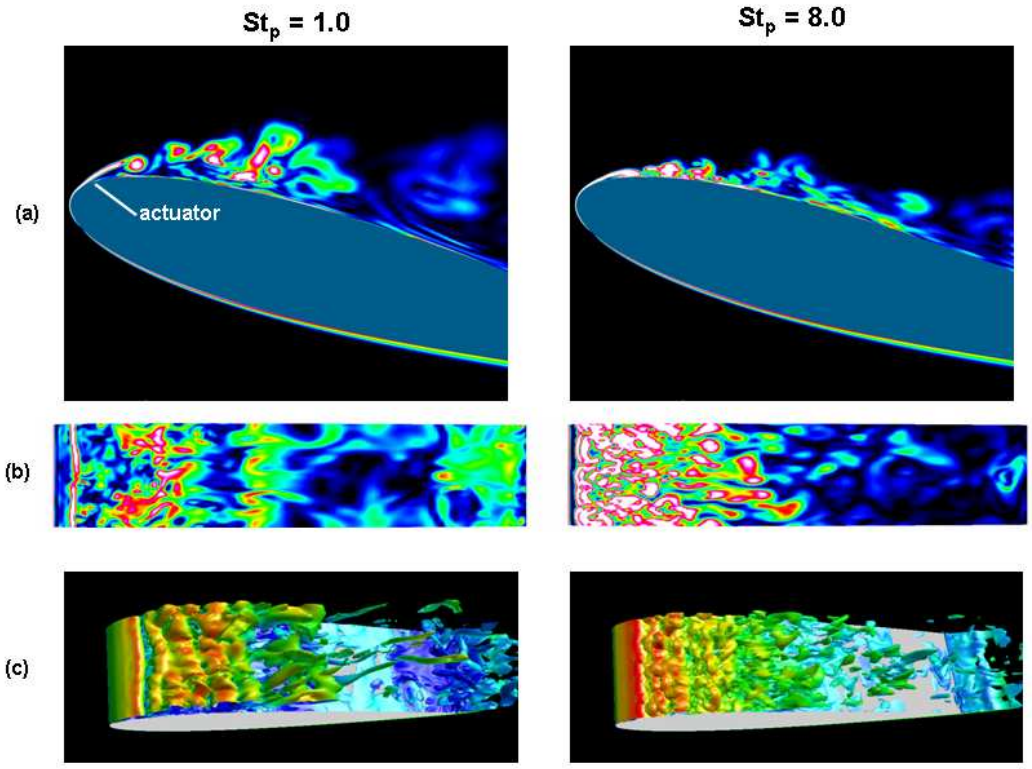

Figure 5. Effect of pulsing frequency of counter-flow DBD actuator on stalled flow above a NACA 0015 wing section ($Re_c = 4.5 \times 10^4, \alpha = 15^o$): instantaneous vorticity magnitude on (a) vertical plane and (b) plane parallel to airfoil surface; (c) iso-surface of vorticity magnitude colored by streamwise velocity

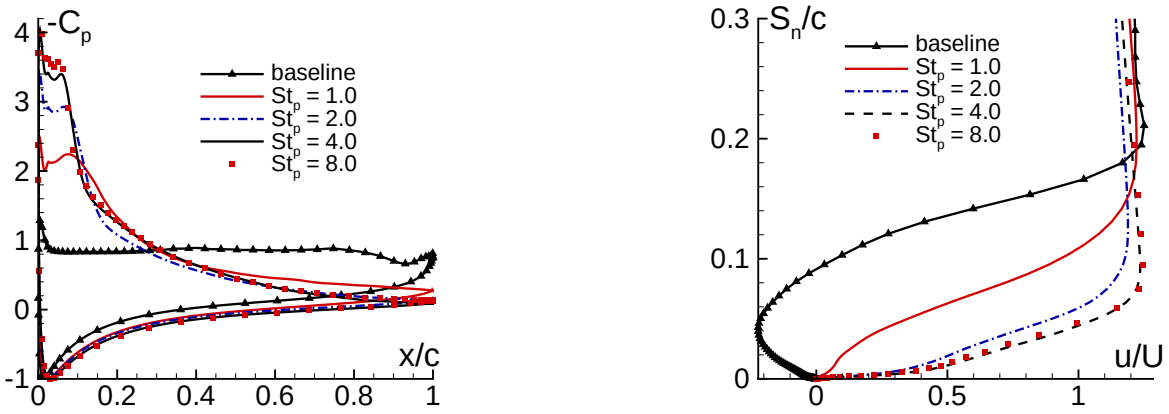

(a) (b)

Figure 6. Effect of pulsing frequency of counter-flow DBD actuator on NACA 0015 airfoil flow ($Re_c = 4.5 \times 10^4, \alpha = 15^o, D_c = 150.0$): (a) mean surface pressure and (b) mean streamwise velocity profile near mid-chord

B. Control of Wing Stall Using a First-Principles Approach

As previously noted, in addition to the duty-cycle forcing, there is also unsteadiness associated with the radio frequency excitation itself. This very high-frequency forcing (typically in the range $1-10kHz$) may have the potential to activate complex flow dynamics even without an imposed duty cycle. A simulation reproducing the unsteadiness of the cycle is therefore essential in order to distinguish the different forcing mechanisms.

A completely *fully-coupled* self-consistent solution of both plasma and fluid phenomena, while attractive, is not currently feasible. The two main reasons are the overwhelming computer resource requirements of 3-D turbulent simulations at plasma time scales, as well as gaps in current understanding of the molecular processes that dominate charged particle generation and behavior. For these reasons, in the present work a *loosely-coupled* approach is employed to accomplish this objective.[12,13] Specifically, the force field is obtained from a separate calculation modeling the near-wall flow in a quiescent medium and then scaled and transferred to the wing section. The implicit assumption is therefore that the intermolecular near-wall processes are not sensitive to the outer flow. This requires that the fluid density and pressure, or collisionality, are relatively high. This is a reasonable expectation for the low-speed atmospheric pressure incompressible flows of interest.

The space charge and electric field distributions, which provide the body force, are obtained in a self-consistent fashion following the procedure described in Refs.[10,26] Briefly, a two-dimensional three-species collisional plasma-sheath model which includes the charge and momentum continuity equations, and Gauss' law for electric potential is employed. Since air chemistry for the pertinent processes in the discharge remain poorly understood, the charge and electric field distributions are obtained under the assumption that the working gas is helium. The governing equations are solved with the multiscale ionized gas (MIG) flow code, developed at the Computational Plasma Dynamics Laboratory at Kettering University. The method is based on a versatile finite-element (FE) procedure adapted from fluid dynamics to overcome the stiffness of the equations generated by multi-species charge-separation phenomena. Further details may be found in Refs. 26–28.

The instantaneous force field distribution obtained from the ionized gas code is stored at several phases during the cycle. This force is then transferred onto the wing mesh employing an area-weighted interpolation procedure, as decribed in Refs. 12 and 13. Linear interpolation is also used in time between the adjacent stored phase angles. A detailed description of the instantaneous force field over a cycle is provided in Ref. 12. The time-averaged body force is predominantly directed downstream and towards the airfoil surface. In order to permit a comparison with the phenomenological approach, the instantaneous force is normalized by its peak value during the cycle, and re-scaled using the actuator strength parameter D_c previously introduced.

In the case described below, the computational mesh employed for the phenomenological approach is retained. However, the non-dimensional time-step is reduced significantly (to 5×10^{-5}) in order to resolve with approximately 95 time steps the radio-frequency oscillation period. The prescribed actuator $5kHz$ signal corresponds to a non-dimensional frequency $St = f_{rf}c/U_\infty = 213$ in terms of flow scales. This value is approximately 27 times larger that the highest pulsing frequency considered in Section IV.A with the phenomenological model.

Results computed with the first-principles approach for a co-flow actuator with a strength parameter $D_c = 240.0$ are shown in Figs. 7 and 8. Comparison of the overall flow field structure with the baseline case shows that the high-frequency forcing associated with continuous actuator operation also promotes transition to turbulence (Fig. 7e). Although separation is not completely eliminated, a significant reduction in the size of the separated region above the airfoil is observed (Fig. 7c). The corresponding mean surface pressure developes a suction peak (Fig. 8a), and a much fuller velocity profile is seen near mid-chord (Fig. 8b).

For the case of continuous operation, it is apparent that the phenomenological approach, which assumes a time-invariant force, cannot reproduce the transition/turbulence enhancements associated with unsteady forcing in the continuously-powered actuator. This is evident in Fig. 8 which shows significantly improved control effectiveness for the first-principles computation relative to the empirical model.

Comparison of the results obtained with the first-principles high-frequency (monochromatic) forcing with the pulsed cases of Section IV.A indicates that the duty cycle (with sufficiently high pulsing frequency St_p) provides a significant improvement in control effectiveness, even for smaller values of D_c. This may be due to the fact that the flow is more receptive to the intermediate forcing frequencies ($2.0 \leq St_p \leq 8.0$) rather that the extremely high radio

frequency itself ($St = 213$). Future computations with a duty cycle using the first-principles approach are required to validate this conclusion and to further assess the merits of the phenomenological model for the case of pulsed actuators.

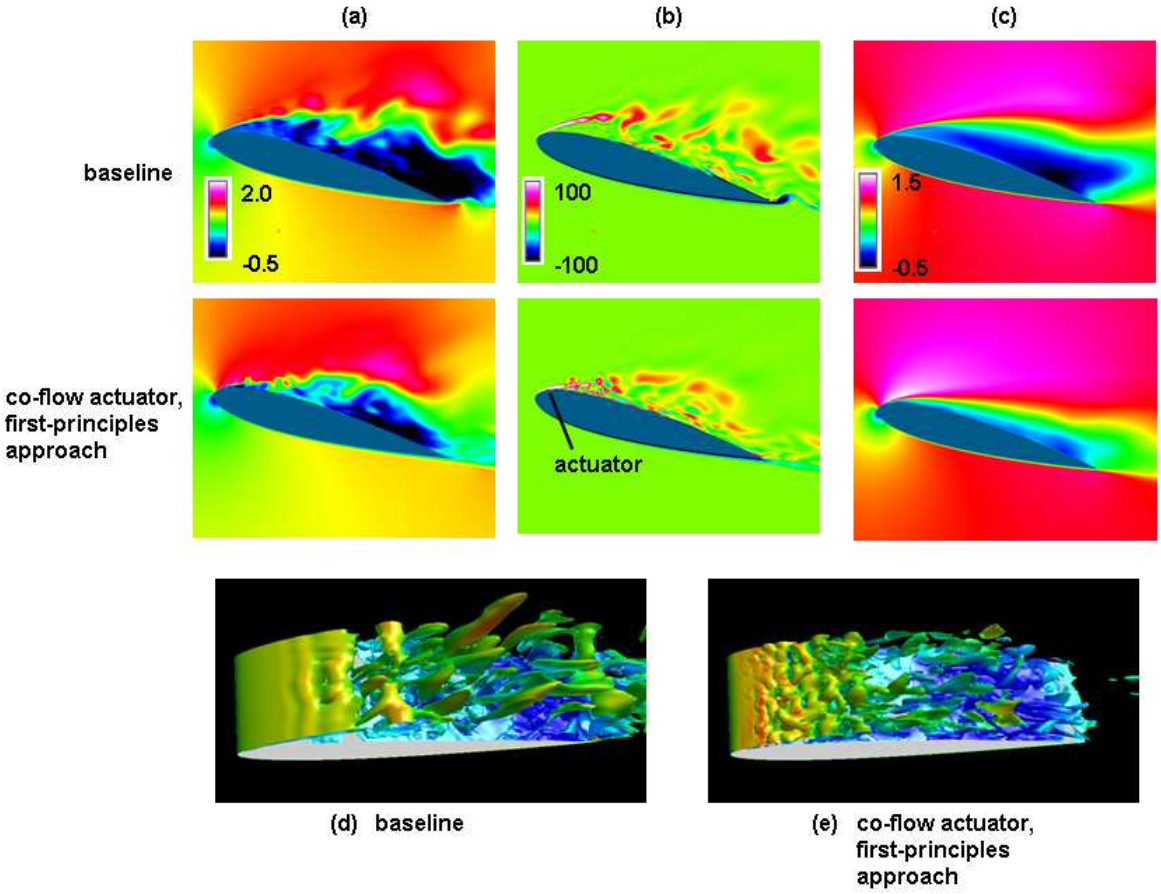

Figure 7. Simulation of continuously-powered co-flow DBD actuator using first-principles approach (NACA 0015,$Re_c = 4.5 \times 10^4, \alpha = 15^o, D_c = 240.0$): (a) instantaneous streamwise velocity, (b) instantaneous spanwise vorticity, (c) mean streamwise velocity; and iso-surface of vorticity magnitude for (d) baseline and (e) controlled cases

C. Tripping of a Laminar Boundary Layer Using a Counter-Flow Actuator

The next case studied corresponds to a flat-plate laminar boundary layer with a steady DBD actuator oriented against the incoming flow. This case is considered since as it will be shown in the following section, tripping of a laminar boundary layer upstream of a region of adverse pressure gradient is of potential utility in the control of unsteady separation.

Implicit Large-Eddy simulations (*ILES*) were performed for a boundary layer developing over a flat plate. The specified Mach number and Reynolds number are $M_\infty = 0.1$ and $Re_{\delta_o} = 1.2 \times 10^4$, where δ_o denotes the incoming nominal laminar boundary layer thickness. The following counter-flow DBD actuator parameters were prescribed:

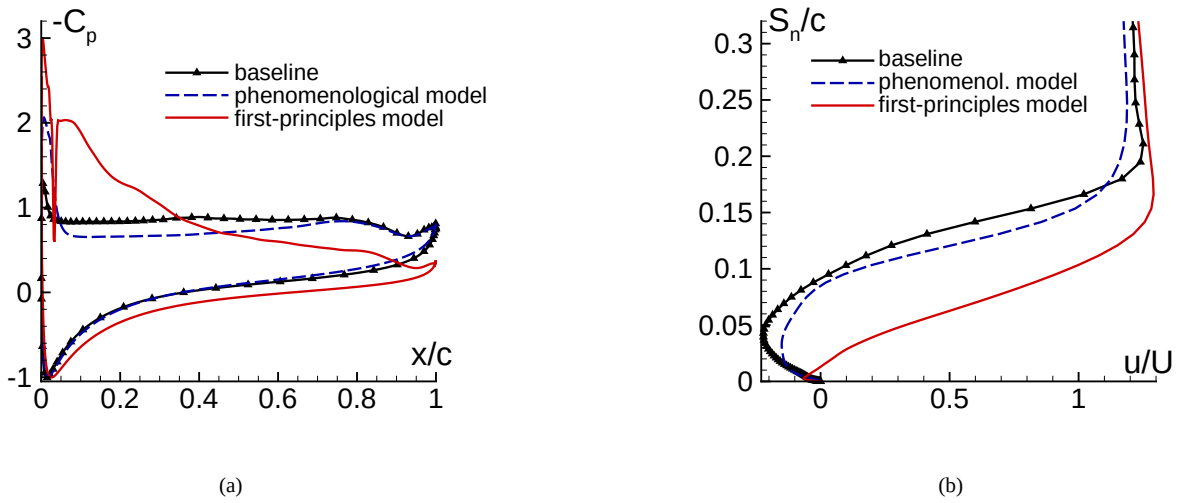

(a) (b)

Figure 8. Comparison of phenomenological and first-principles approaches for continuously-powered co-flow DBD actuator on a NACA 0015 wing section ($Re_c = 4.5 \times 10^4, \alpha = 15^o$): (a) mean surface pressure and (b) mean streamwise velocity profile near mid-chord

$a/\delta_o = 0.025, b/\delta_o = 0.125$, and $D_c = 20.0$. The actuator origin is located at $x/\delta_o = 2.6$. Computations were performed on a non-uniform Cartesian grid with $625 \times 93 \times 76$ points in the streamwise, normal and spanwise directions respectively. The flow was assumed to be periodic in the spanwise direction over a width equal to $0.71\delta_o$. In the region downstream of transition, typical values of the grid spacing in terms of wall units are $\Delta x^+ \approx 40.0, \Delta {y_w}^+ \approx 0.9$ and $\Delta z^+ \approx 26.0$.

The instantaneous flow structure is shown in Fig. 9. Contours of streamwise velocity on a horizontal plane at $y^+ \approx 10.0$ (Fig. 9a) show that a small region of separation is created by the focused upstream-pointed wall jet generated by the counter-flow actuator. Although no unsteady forcing is applied, this separation region is subject to spanwise instabilities which quickly promote transition to turbulence. Therefore in this application, the DBD actuator may be viewed as a controllable (on-demand) boundary-layer tripping device. The abrupt onset of transition can be clearly observed in the contours and iso-surface of vorticity magnitude shown in Figs. 9c,d.

The streamwise evolution of the boundary layer along the plate is presented in Fig. 10 in terms of the distribution of spanwise-averaged mean skin-friction coefficient and momentum thickness. Following the small region of separation, C_f rises sharply and reaches its new turbulent levels in an approximate distance of $12\delta_o$ downstream of the actuator. The momentum thickness (θ) drops sharply over the actuator and begins to display a fairly linear growth starting at approximately $x/\delta_o = 7.5$. At $x/\delta_o = 35.0$, the computed Reynolds number based on θ is approximately 3300, and the corresponding boundary layer shape factor is 1.35.

The spanwise-averaged mean velocity profile and rms velocity fluctuations are shown in Fig. 11. The mean velocity in terms of wall coordinates appears to be approaching the case of an equilibrium zero-presssure-gradient turbulent boundary layer, although some discrepancies still exist in the log-region. The relaxation of the boundary layer towards equilibrium following bypass transition is more apparent in the evolution of the streamwise velocity fluctuations (Fig. 11b). Closer to the DBD actuator, the rms fluctuations exhibit a double peak which is also observed in experiments of bypass transition (*e.g.*, Ref. 29). This second peak diminishes as an equilibrium state is approached.

The present results indicate that even with small values for the actuator strength parameter, a steady counter-flow DBD actuator can be an effective on-demand tripping device for a laminar boundary layer. This property is exploited in the control of laminar boundary layer separation described in the following section.

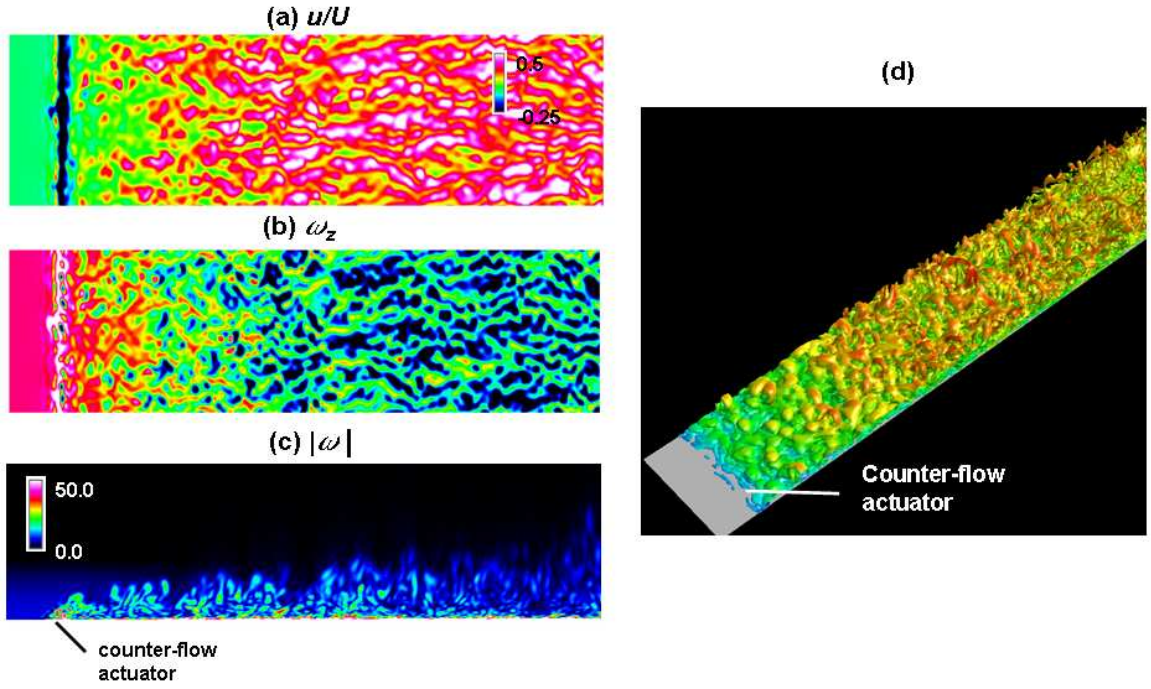

Figure 9. Instantaneous flow structure for a steady counter-flow actuator in a laminar boundary layer: (a) streamwise velocity and (b) spanwise vorticity on a horizontal plane ($y^+ \approx 10.0$); (c) vorticity magnitude on a vertical plane and (d) iso-surface of vorticity magnitude

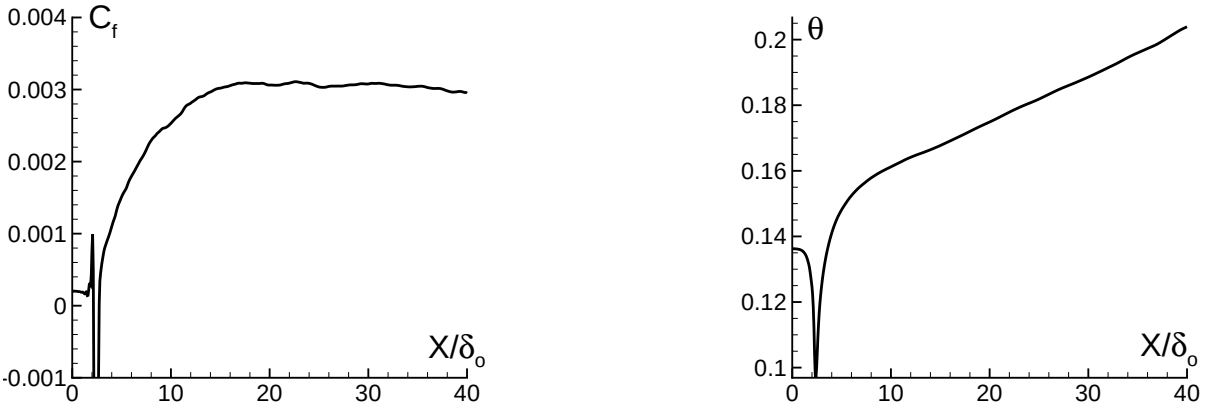

(a) (b)

Figure 10. Streamwise evolution of (a) the mean skin-friction coefficient and (b) mean boundary-layer momentum thickness dowstream of steady counter-flow actuator on a flat plate

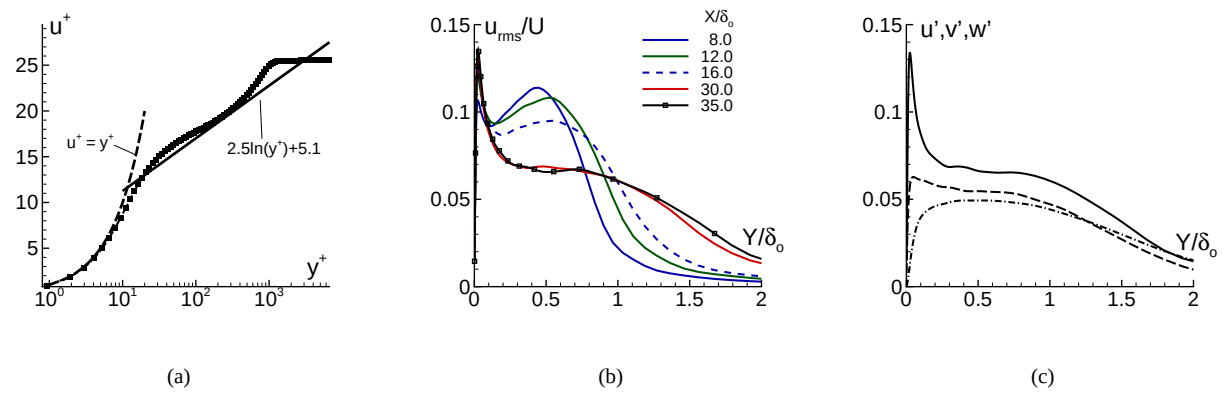

(a) (b) (c)

Figure 11. Effect of steady counter-flow actuator on a transitional flat-plate boundary layer: (a) Mean streamwise velocity profile at $x/\delta_o = 35.0$, (b) evolution of streamwise velocity fluctuations, and (c) turbulent fluctations at $x/\delta_o = 35.0$

D. Control of Laminar Separation Over a Ramp

This case considers the control of laminar boundary-layer separation over a generic ramp configuration (Fig. 12). This simple geometry is taken as a model problem of separation near the trailing edge of a natural laminar flow wing section. The flow conditions are Mach number $M_\infty = 0.1$ and Reynolds number (based on the ramp length c) $Re_c = 6.0 \times 10^4$. The incoming boundary layer is assumed to be laminar upstream of the ramp, with nominal thickness $\delta_o/c = 0.0625$. To facilitate grid generation, the ramp shape was specified analytically using a simple half-cosine function with a height $h/c = 0.325$. Computations were performed on a grid containing $416 \times 131 \times 79$ points in the streamwise, normal and spanwise directions respectively. The flow was assumed to be periodic in the spanwise direction with a width equal to $0.25c$. A non-dimensional time step $\Delta t U_\infty/c = 6.25 \times 10^{-4}$ was specified corresponding to approximately 500 steps per duty cycle.

The baseline instantaneous and time-averaged flow field structure is shown in Figs. 12 and 13 respectively. The incoming steady laminar boundary layer is observed to separate immediately upon encountering the ramp (Fig. 12a), and a large time-averaged re-circulation region of approximate streamwise extent $2.2c$ is formed (Figs. 13b,d). The mean surface pressure distribution is characterized by an extensive plateau region (Fig. 14a). Examination of the countours of vorticity magnitude (Fig. 12b) shows that after separation, a laminar free shear layer is formed. Subsequently, this shear layer begins to roll-up into coherent spanwise vortices which abruptly breakdown just upstream of re-attachment. This process is reflected in a sharp rise in surface pressure and skin-friction coefficient (Fig. 14). Reynolds stress ($u'v'$) contours, shown in Fig. 13c, display high negative values in the re-attachment region associated with transition to turbulence.

In order to control this massive separation region, we first consider a pulsed co-flow DBD actuator located just upstream of the ramp ($x/c = -0.13$). The following actuator parameters are prescribed: $a/c = 0.0125, b/c = 0.125$, $D_c = 150.0$, and $St_p = 3.2$. In terms of the mean baseline separation length, this non-dimensional duty-cycle primary frequency is $F^+ \approx 7.0$. The pulsed actuator has a significant effect on the development of the shear-layer, as seen in Fig. 12. The breakdown process of the shear layer is observed to move closer to the separation point due to the unsteady forcing. As a result of this turbulence enhancement, a significant reduction is achieved in the size of the separation region. The mean re-attachemnt location moves from $x/c = 2.2$ to $x/c = 1.65$. The surface pressure also exhibits a more rapid recovery and a much shorter pressure plateau. The reduction of the vertical extent of the reversed-flow region can also be seen in the mean streamwise velocity profiles shown in Figs. 15b,c. The effect of the pulsed actuator on the turbulent flow structure is examined in terms of the Reynolds stress (Fig. 13c). There is actually a reduction in the magnitude of the Reynolds stress relative to the baseline flow situation. In addition, the region of significant values of $u'v'$ is displaced downward and upstream tracking the development of the forced shear layer.

As was shown in the previous section, a low-power counter-flow DBD actuator can be used as an effective boundary-layer tripping device. Therefore, we now consider the use of this strategy for the control of the separated flow over the ramp since as it is well known a turbulent incoming boundary layer is capable of sustaining a higher adverse pressure gradient. For this purpose, instead of employing a pulsed actuator near the separated laminar shear layer, we use a steady counter-flow actuator to promote boundary-layer transition to turbulence *upstream* of the ramp. The actuator is located at $x/c = -0.75$ and the paremeters $a/c = 0.0125, b/c = 0.125, D_c = 25.0$ are prescribed. As observed in Figs. 12b,c, the laminar boundary layer begins to transition downstream of the counter-flow actuator. At the station $x/c = -0.17$, the mean streamwise velocity profile (Fig. 15a) exhibits, as expected, a much fuller profile near the wall. This allows the flow to turns downward upon encountering the ramp without significant boundary-layer separation (Fig. 13d). The time-averaged surface pressure (Fig. 14a) displays a pronounced suction peak near $x/c = 0.0$ corresponding to the well-defined expansion region at the bend (Fig. 13a). Following this expansion, the surface pressure exhibits a sharp recovery without a noticeable plateau. The mean streamwise velocity profiles (Figs. 15b,c) demonstrate a dramatic improvement in the flow downstream of the ramp. The flow is now practically re-attached, with the exception of a much smaller time-averaged separation bubble at the end of the ramp. Contours of Reynolds stress (Fig. 13c) show the tripping of the boundary layer by the counter-flow actuator. In the region above the ramp, the Reynolds stress decreases relative to the baseline and pulsed actuator cases.

These exploratory results clearly demonstrate that for separated laminar flows (encountered in off-design operation of laminar flow wings and low-pressure turbines) improved control may be achieved through modification of the boundary layer sufficiently upstream of the adverse pressure gradient region. In this manner, supression of massive separation can be obtained with a significant reduction in the actuator power requirements. This may also provide scalability to higher freestream velocities encountered in practical applications. Although unsteady forcing of the separated shear layer provides control of the reversed flow region, the required actuator strength parameter has to be an order of magnitude larger than that needed for tripping the boundary layer.

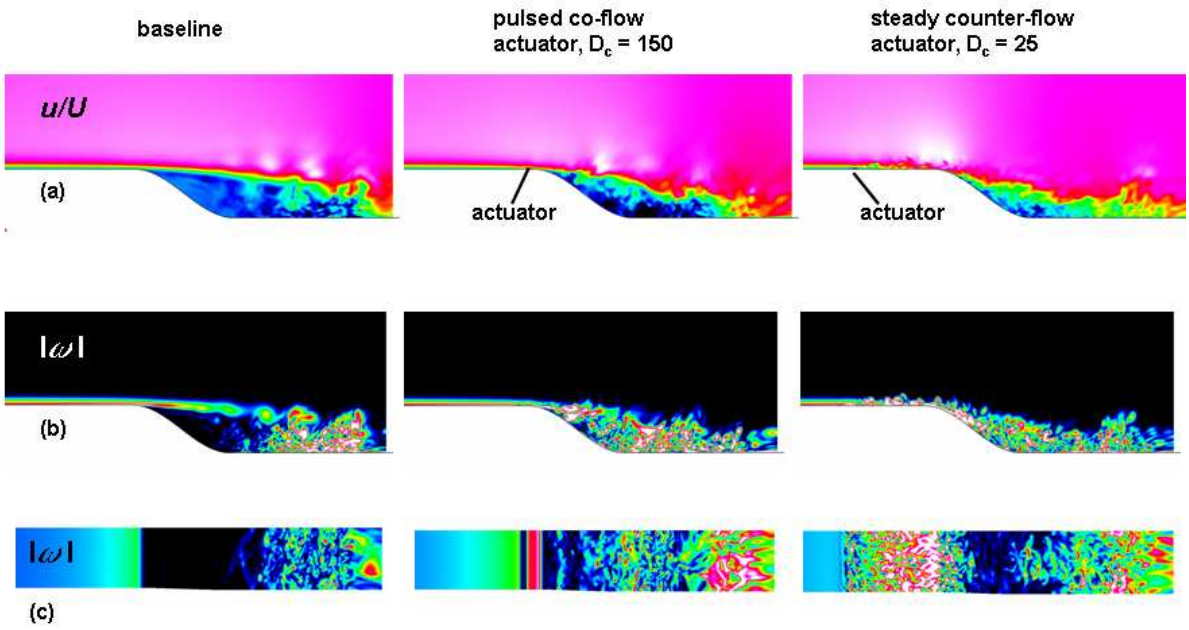

Figure 12. Effect of DBD actuator on instantaneous flow structure over a separation ramp: (a) streamwise velocity, and vorticity magnitude on (b) vertical plane and on (c) computational grid surface above the wall

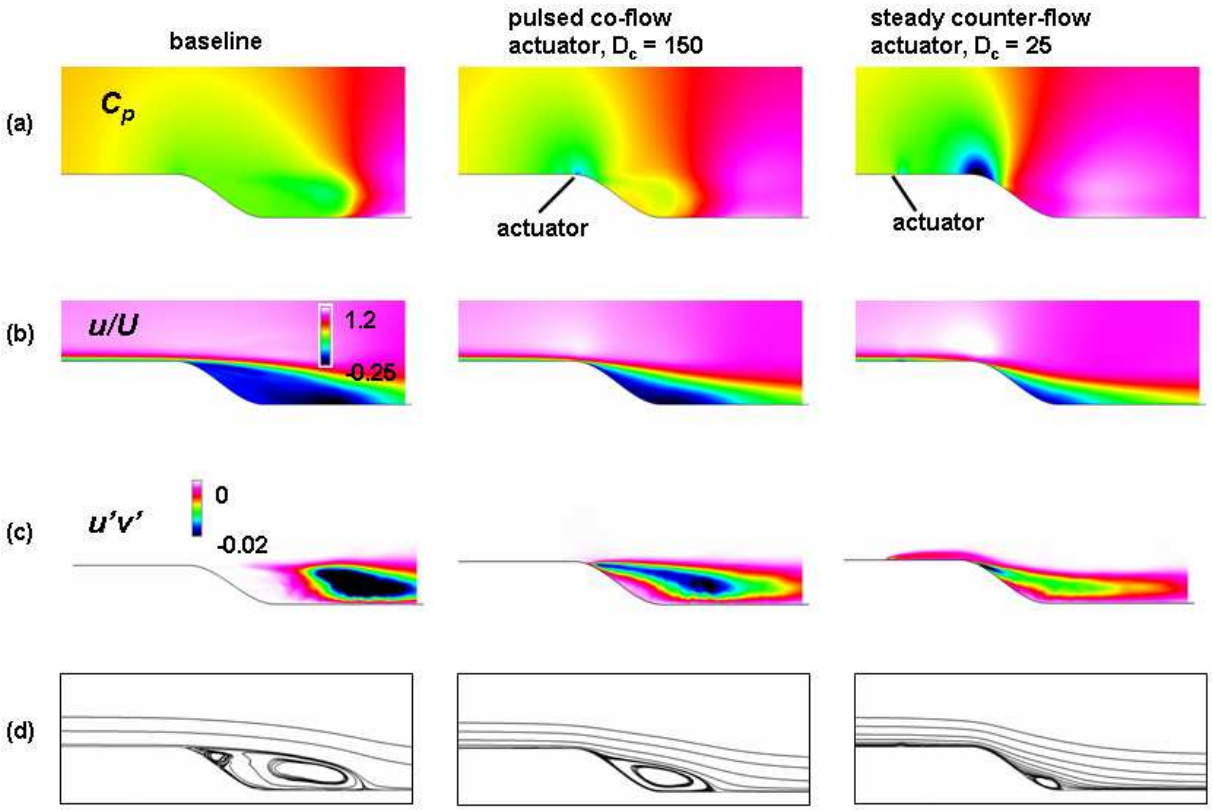

Figure 13. Effect of DBD actuator on time-averaged flow structure over a separation ramp: (a) static pressure, (b) streamwise velocity, (c) Reynolds stress, and (d) streamlines in separation region

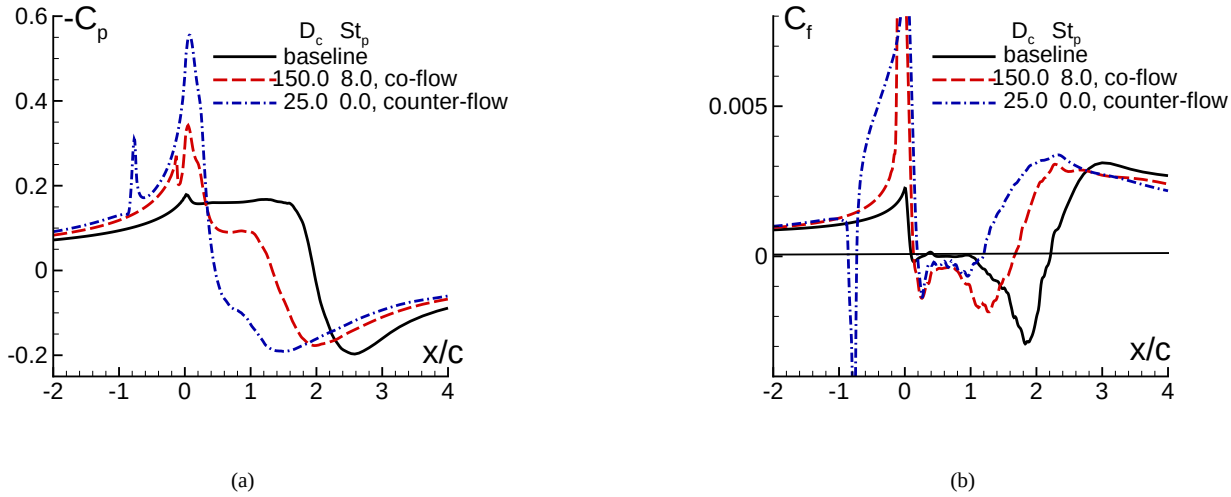

(a) (b)

Figure 14. Effect of DBD actuator on separated flow over ramp: (a) mean surface pressure and (b) skin-friction coefficient

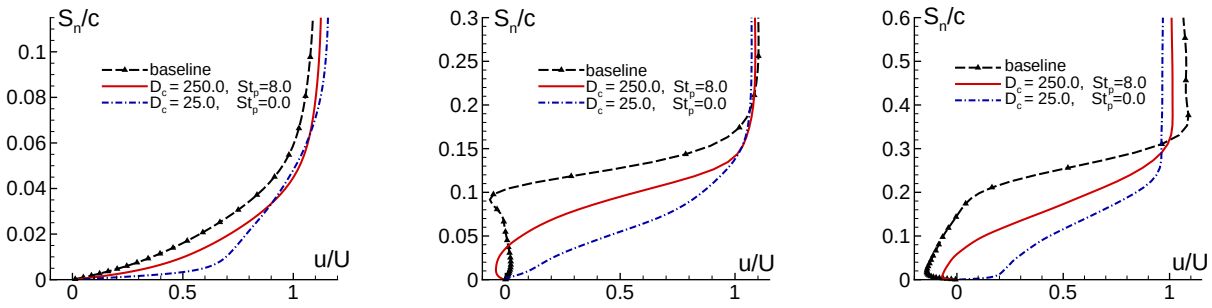

Figure 15. Mean streamwise velocity profiles for flow over a separation ramp: (a) $x/c = -0.17$**, (b)** $x/c = 0.43$**, and (c)** $x/c = 1.43$

E. Control of Turbulent Separation Over a Wall-Mounted Hump

The last case considered is that of turbulent separation over a wall-mounted hump (Fig. 16). This geometry is selected for two main reasons. First, this configuration has been the subject of several experimental and computational studies of flow control employing both steady suction and oscillatory blowing.[30–32] Second, it permits and exploration of the use of DBD actuators for the control of *turbulent* rather than *laminar/transitional* boundary-layer separation considered earlier.

The hump geometry simulates the upper surface of a 20%-thick Glauert-Goldschmied airfoil section. The flow conditions were prescribed as $M_\infty = 0.1$ and chord Reynolds number 1.5×10^5. The computational mesh was generated by redistributing the grid lines of an existing mesh employed previously in a computational flow control study.[32] The grid has dimensions $654 \times 131 \times 79$ in the streamwise, vertical and spanwise directions respectively. The flow was assumed to be periodic in the spanwise direction with an extent of $0.1c$. A non-dimensional time step $\Delta t U_\infty/c = 0.00025$ was used which provided 500 steps per duty-cycle.

At inflow (see Fig. 16), an incoming laminar boundary layer is prescribed with nominal thickness $\delta_o = 0.05c$. In order to study turbulent separation, the boundary layer was tripped ahead of the hump leading edge using a steady counter-flow DBD actuator, as described earlier. The actuator was located at $x/c = -1.0$ with parameters $a/c = 0.005, b/c = 0.05$ and $D_c = 25.0$. As shown in Fig. 16, this actuator induces transition of the initially laminar boundary layer upstream of the hump and provides more realistic inflow conditions for all subsequent simulations.

The unsteady and time-averaged flow structure for the baseline case are presented in Figs. 17 and 18 respectively. The baseline flow is characterized by unsteady separation and by the formation of a mean recirculation zone over the aft-portion of the hump. The mean surface pressure distribution (Fig. 19a) displays a well-defined suction peak and a pressure plateau associated with the separated region. These overall features are in qualitative agreement with previous experiments and computations obtained at higher Reynolds numbers and for a different turbulent boundary-layer thickness upstream of the hump.[30,32]

In order to control the extent of separation, a second DBD actuator is employed located at $x/c = 0.6$, just upstream of the detachment point (Fig. 16). This simulated pulsed co-flow actuator is prescribed using the following parameters: $a/c = 0.005, b/c = 0.05$, and $St_p = 8.0$. Computations with an actuator strength $D_c = 500.0$ (not shown) essentially eliminated the separation region. However, of more interest in the present study, are results achievable with smaller values of D_c. For $D_c = 250.0$, a significant reduction in the separation zone is observed (Figs. 18b,d). The mean re-attachment point is shifted from $x/c = 1.19$ to $x/c = 0.93$. Also, the normal extent of the reversed flow region is reduced considerably. This process is accompanied by the development of a more pronounced expansion region over the hump, as seen in the mean pressure countours (Fig. 18a) and in the corresponding C_p distribution (Fig. 19a). A plateau in the C_p curve is no longer evident and a rapid recovery in surface pressure is observed. A comparison of the

time-averaged streamwise velocity profiles at select locations is shown in Fig. 20. The control case clearly exhibits a fuller profile upstream of separation and a better recovery downstream of re-attachment. The impact of actuation on the turbulent stress is shown in Fig. 18c. Forcing results in a reduced overall region of high negative Reynolds stress due to the smaller separation zone. However, just downstream of the actuator, a significant increase in the magnitudes of $u'v'$ is observed.

Lowering the actuator strength parameter further to $D_c = 150.0$ still provided some reduction of the separation zone (Fig. 18d). However, control effectiveness is diminished significantly. The surface pressure still displays a higher suction peak and a less pronounced plateau relative to the baseline flow. A fuller mean velocity profile is also observed downstream of re-attachment (Fig. 20c).

These results seem to suggest that in order to achieve sufficient control when the boundary layer is already in a *turbulent* state, the actuator amplitude must be above a certain threshold level. This is in contrast with the control of separation over the airfoil described previously in Section IV.A, wherein control effectiveness could be achieved with much lower values of D_c. This behavior is expected since the laminar/transitional boundary layer is very receptive to the imposed small-amplitude disturbances. These findings are in qualitative agreement with other control techniques for separated turbulent flows (*e.g.* control of weapon bay cavities using high-frequency pulsed blowing[33]) where sufficiently high levels of actuation must be employed in order to achieve effective control. Furthermore, the higher actuator strength requirements have implications for the scalability of these devices to flight situations.

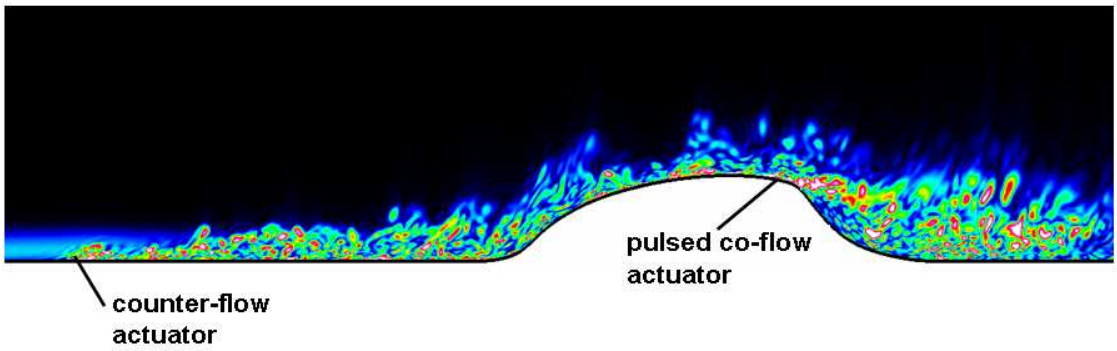

Figure 16. Control of turbulent separation over a wall-mounted hump

V. CONCLUDING REMARKS

A computational exploration has been conducted of the effects of radio-frequency dielectric barrier discharge (DBD) actuators on transitional and turbulent separated flows. A high-order Navier-Stokes solver, augmented with either a phenomenological or a loosely-coupled first-principles model representing the plasma-induced body forces is employed. Several applications are considered, including wing stall suppression, control of boundary layer transition on a plate, control of laminar separation over a ramp, and turbulent separation over a wall-mounted hump.

Suppression of wing stall was demonstrated using either a co-flow or a counter-flow pulsed actuator located near the airfoil leading edge. With the phenomenological approach, control effectiveness was achieved with high pulsing frequencies for moderate values of the actuator strength parameter. For the Reynolds number considered, suitable control is achieved for relatively low values of actuator strength since the separated laminar/transitional shear layer is highly receptive to such imposed disturbances. By contrast, a steady actuator force of the same magnitude provided little control of separation. These results highlight the greater importance of transition/turbulence enhancement versus pure streamwise momentum injection as the primary control mechanism. From a computational standpoint, this also mandates the use of full three-dimensional large-eddy simulations capable of capturing the interaction of the unsteady plasma forces with the turbulent structure.

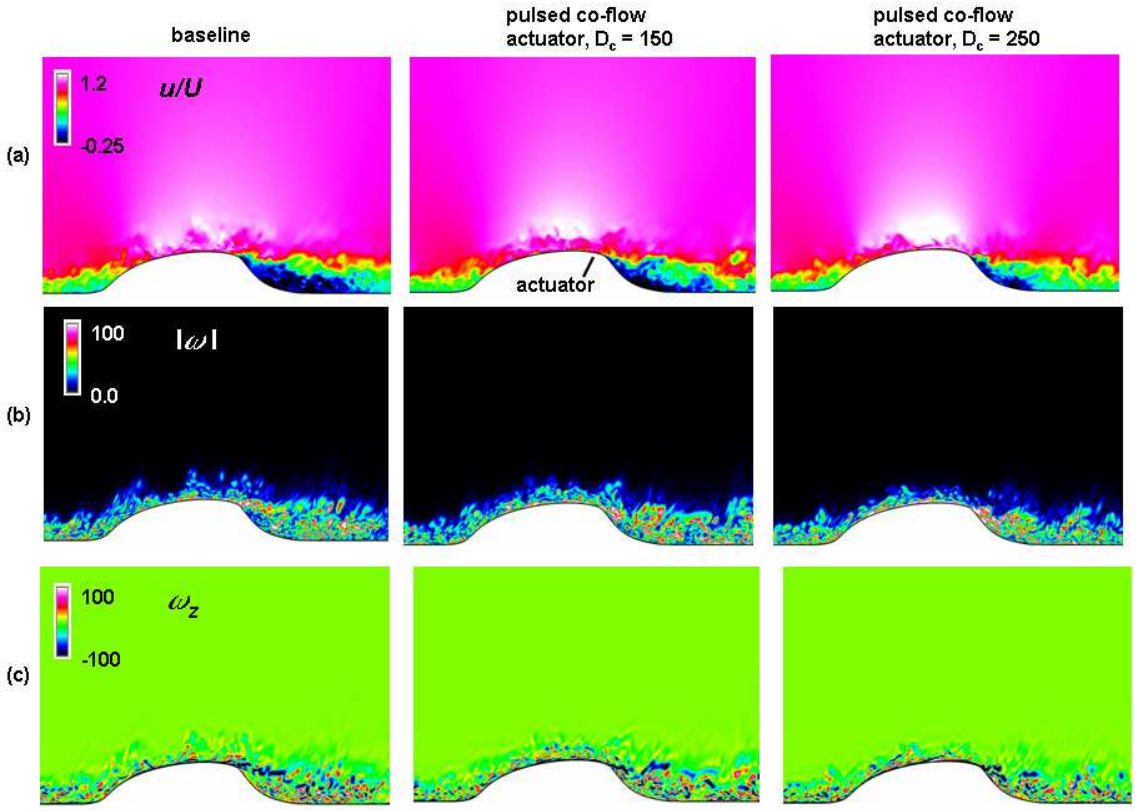

Figure 17. Effect of pulsed co-flow DBD actuator on instantaneous flow structure over a wall-mounted hump: (a) streamwise velocity, (b) vorticity magnitude, and (c) spanwise vorticity component

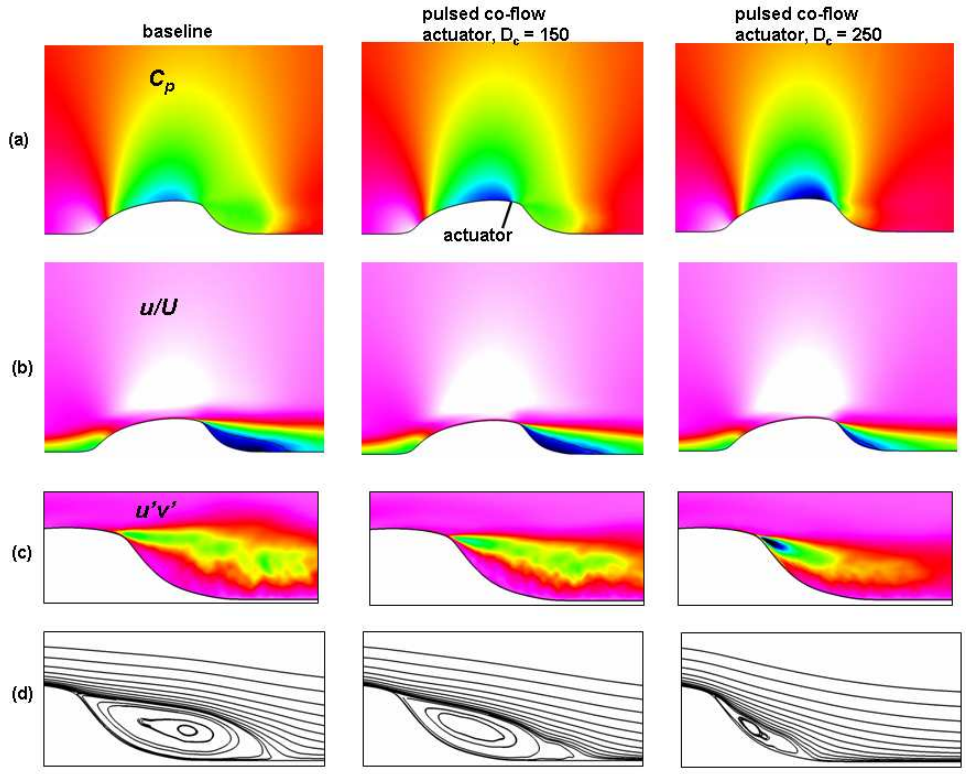

Figure 18. Effect of pulsed co-flow DBD actuator on time-averaged flow structure over a wall-mounted hump: (a) static pressure, (b) streamwise velocity, (c) Reynolds stress, and (d) streamlines in separation region

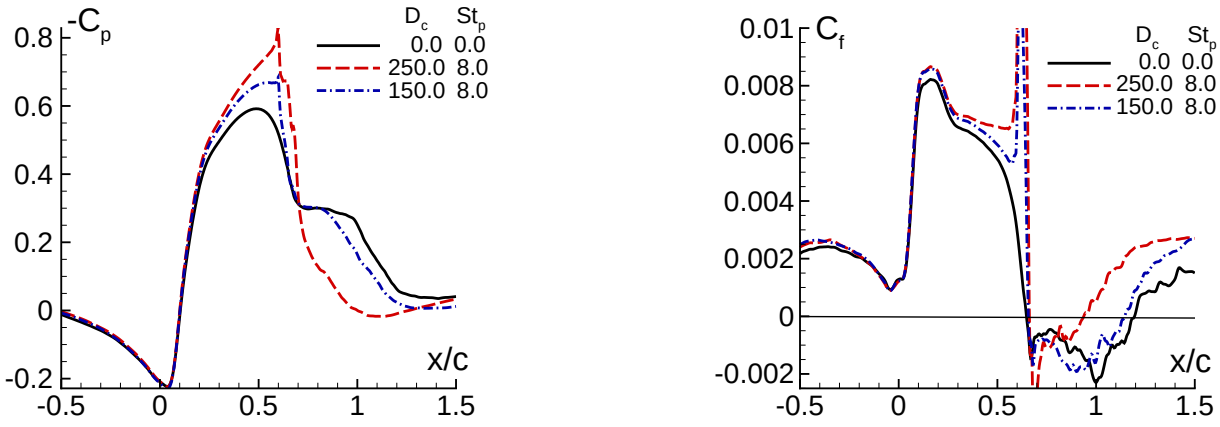

(a) (b)

Figure 19. Effect of pulsed co-flow DBD actuator on separated flow over a wall-mounted hump: (a) mean surface pressure and (b) skin-friction coefficient

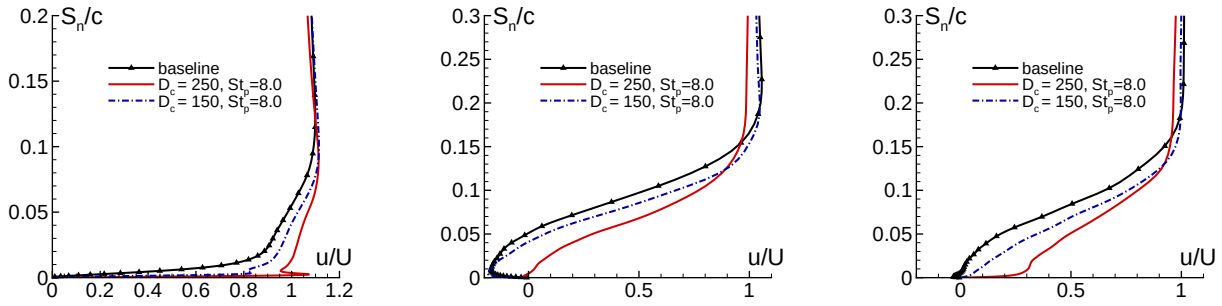

Figure 20. Mean streamwise velocity profiles for flow over a wall-mounted hump: (a) $x/c = 0.65$**, (b)** $x/c = 0.9$**, and (c)** $x/c = 1.15$

The first-principles approach was employed for the case of wing stall suppression using a continuously-powered co-flow actuator. For continuous actuator operation, the first-priciples model is needed in order to reproduce the effects of the inherently unsteady radio-frequency force induced by the plasma actuator. The pulsed-modulated unsteady plasma force used in the phenomenological model is found to be more effective than the first-principles monochromatic radio-frequency forcing. This may be due to the fact that the flow is more receptive to intermediate forcing frequencies rather that the extremely high radio frequency itself. Future computations with a duty cycle using the first-principles approach are planned to validate this conclusion and to further assess the merits of the phenomenological model for the important case of pulsed actuators.

The use of a counter-flow DBD actuator with relatively low strength was shown to provide an effective on-demand tripping device for a laminar boundary layer developing along a flat plate. This property is exploited for the suppression of laminar separation over a ramp. In this case, tripping the boundary layer just upstream of the adverse pressure gradient region provides a very effective means of reducing separation. This strategy is found to be more effective than the use of a pulsed actuator of higher strength placed near the separation point. These results may be of potential application in the control of separation for natural laminar flow airfoils and low-pressure turbines in off-design operation.

Finally, control of turbulent boundary-layer separation over a wall-mounted hump suggests that once the flow is turbulent, control effectiveness is only achieved provided the actuator strength exceeds a certain threshold. This finding has implications for the scalability of DBD devices to higher freestream velocities encountered in practical applications.

ACKNOWLEDGMENTS

The authors are grateful for AFOSR sponsorship under tasks monitored by Lt.Col R. Jefferies, Dr. J. Schmisseur and Dr. F. Fahroo. This work was also supported in part by a grant of HPC time from the DoD HPC Shared Resource Centers at ASC, ERDC and NAVO.

References

[1] M.L. Post and T.C. Corke. Separation control on high angle of attack airfoil using plasma actuators. *AIAA Paper 2003-1024*, 2003.

[2] T.C. Corke and M.L. Post. Overview of plasma flow control: Concepts, optimization and applications. *AIAA Paper 2005-0563*, 2005.

[3] J.R. Roth. Aerodynamic flow acceleration using paraelectric and peristaltic electrohydrodynamic (ehd) effects of a one atmosphere uniform glow discharge plasma (oaugdp). *Phys. Plasmas*, 10:2117, 2003.

[4] T.C. Corke, E.J. Jumper, M.L. Post, D. Orlov, and T.E. McLaughlin. Application of weakly-ionized plasmas as wing flow-control devices.

AIAA Paper 2002-0350, Jan. 2002.

[5] M. Post and T. Corke. Separation control using plasma actuators - dynamic stall control on an oscillating airfoil. *AIAA Paper 2004-2517*, June 2004.

[6] J. List, A.R. Byerley, T.E. McLaughlin, and R. VanDyken. Using plasma actuators flaps to control laminar separation on turbine blades in a linear cascade. *AIAA Paper 2003-1026*, Jan. 2003.

[7] V. Voikov, T. Corke, and O. Haddad. Numerical simulation of flow control over airfoils using plasma actuators. *Bulletin of the APS*, 2004.

[8] W. Shyy, B. Jayaraman, and A. Andersson. Modeling of glow-discharge induced fluid dynamics. *J. Appl. Phys.*, 92:6434, 2002.

[9] S. Roy and D. Gaitonde. Ionized collisional flow model for atmospheric rf application. *AIAA Paper 2004-2354*, 2004.

[10] S. Roy and D. Gaitonde. Multidimensional collisional dielectric barrier discharge for flow control at atmospheric pressures. *AIAA Paper 2005-4631*, 2005.

[11] D.V. Gaitonde, M.R. Visbal, and S. Roy. Control of flow past a wing section with plasma-based body forces. *AIAA Paper 2005-5302*, 2005.

[12] D.V. Gaitonde, M.R. Visbal, and S. Roy. A coupled approach for plasma-based flow control simulations of wing sections. *AIAA Paper 2006-1205*, 2006.

[13] D.V. Gaitonde, M.R. Visbal, and S. Roy. Three-dimensional plasma-based stall control simulations with coupled first-principles approaches. *ASME Paper FEDSM2006-98553*, 2006.

[14] D.A. Anderson, J.C. Tannehill, and R.H. Pletcher. *Computational Fluid Mechanics and Heat Transfer*. McGraw-Hill Book Company, 1984.

[15] M.R. Visbal and D.V. Gaitonde. High-Order Accurate Methods for Complex Unsteady Subsonic Flows. *AIAA Journal*, 37(10):1231–1239, 1999.

[16] D.V. Gaitonde and M.R. Visbal. High-Order Schemes for Navier-Stokes Equations: Algorithm and Implementation into FDL3DI. Technical Report AFRL-VA-WP-TR-1998-3060, Air Force Research Laboratory, Wright-Patterson AFB, 1998.

[17] S.K. Lele. Compact Finite Difference Schemes with Spectral-like Resolution. *Journal of Computational Physics*, 103:16–42, 1992.

[18] D.V. Gaitonde, J.S. Shang, and J.L. Young. Practical Aspects of Higher-Order Numerical Schemes for Wave Propagation Phenomena. *Int. Jnl. for Num. Methods in Eng.*, 45:1849–1869, 1999.

[19] P. Alpert. Implicit Filtering in Conjunction with Explicit Filtering. *J. Comp. Phys.*, 44:212–219, 1981.

[20] D.V. Gaitonde and M.R. Visbal. Further Development of a Navier-Stokes Solution Procedure Based on Higher-Order Formulas. *AIAA Paper 99-0557*, January 1999.

[21] M.R. Visbal and D.P. Rizzetta. Large-Eddy Simulation on Curvilinear Grids Using Compact Differencing and Filtering Schemes. *Journal of Fluids Engineering*, 124:836–847, 2002.

[22] M.R. Visbal, P.E. Morgan, and D.P. Rizzetta. An Implicit LES Approach Based on High-Order Compact Differencing and Filtering Schemes. *AIAA Paper 2003-4098*, June 2003.

[23] M.R. Visbal and D.V. Gaitonde. Control of vortical flows using simulated plasma actuators. *AIAA Paper 2006-0505*, 2006.

[24] M. R. Visbal and J. S. Shang. Investigation of the Flow Structure Around a Rapidly Pitching Airfoil. *AIAA Journal*, 27(8):1044–1051, 1989.

[25] A. Glezer, M. Amitay, and A. Honohan. Aspects of Low- and High-Frequency Actuation for Aerodynamic Flow control. *AIAA Journal*, 43(7):1501–1511, 2005.

[26] S. Roy, K. Singh, H. Kumar, D. Gaitonde, and M. Visbal. Effective discharge dynamics for plasma flow control. *AIAA Paper 2006-0374*, 2006.

[27] D. Balagangadhar and S. Roy. Design sensitivity analysis and optimization of steady fluid-thermal systems. *Computer Methods in Applied Mechanics and Engineering*, 190:5465–5479, Aug. 2001.

[28] S. Roy and B.P. Pandey. Development of a finite element-based hall-thruster model. *J. Prop. Power*, 19:964–975, 2003.

[29] K. Sohn and E. Reshokto. Experimental Study of Boundary Layer Transition with Elevated Free-Stream Turbulence on a Heated Flat Plate. *NASA CR-187068*, 1991.

[30] D. Greenblatt, K.B. Paschal, C.S. Yao, and J. Harris. A separation control cfd validation test case part 2. zero efflux oscillatory blowing. In *AIAA Paper 2005-0485*, January 2005.

[31] C.L. Rumsey, T. Gatski, W.L. Sellers, V.N. Vatsa, and S.A. Viken. Summary of the 2004 computational fluid dynamics validation workshop on synthetic jets. *AIAA Journal*, 44(2):194–207, 2006.

[32] P.E. Morgan, D.P. Rizzetta, and M.R. Visbal. Large-eddy simulation of flow over a wall-mounted hump. In *AIAA Paper 2005-0484*, January 2005.

[33] M. Stanek, G. Raman, V. Kibens, J. Ross, J. Odedra, and J. Peto. Control of Cavity Resonance Through Very High Frequency Forcing. *AIAA Paper 2000-1905*, 2000.